Magnitude of Enhanced Permeability and Retention Effect in Tumors with Different Phenotypes: 89Zr-Albumin as a Model System

Carola Heneweer*[1,2], Jason P. Holland*[3], Vadim Divilov[3], Sean Carlin[4], and Jason S. Lewis[1,3]

[1]Program in Molecular Pharmacology and Chemistry, Memorial Sloan-Kettering Cancer Center, New York, New York; [2]Department of Diagnostic Radiology, University Hospital Schleswig-Holstein, Kiel, Germany; [3]Radiochemistry Service, Department of Radiology, Memorial Sloan-Kettering Cancer Center, New York, New York; and [4]Department of Medical Physics, Memorial Sloan-Kettering Cancer Center, New York, New York

Targeted nanoparticle-based technologies show increasing prevalence in radiotracer design. As a consequence, quantitative contribution of nonspecific accumulation in the target tissue, mainly governed by the enhanced permeability and retention (EPR) effect, becomes highly relevant for evaluating the specificity of these new agents. This study investigated the influence of different tumor phenotypes on the EPR effect, hypothesizing that a baseline level of uptake must be exceeded to visualize high and specific uptake of a targeted macromolecular radiotracer. **Methods:** These preliminary studies use 89Zr-labeled mouse serum albumin (89Zr-desferrioxamine-mAlb) as a model radiotracer to assess uptake and retention in 3 xenograft models of human prostate cancer (CWR22rv1, DU-145, and PC-3). Experiments include PET and contrast-enhanced ultrasound imaging to assess morphology, vascularization, and radiotracer uptake; temporal ex vivo biodistribution studies to quantify radiotracer uptake over time; and histologic and autoradiographic studies to evaluate the intra- and intertumoral distribution of 89Zr-desferrioxamine-mAlb. **Results:** Early uptake profiles show statistically significant but overall small differences in radiotracer uptake between different tumor phenotypes. By 20 h, nonspecific radiotracer uptake was found to be independent of tumor size and phenotype, reaching at least 5.0 percentage injected dose per gram in all 3 tumor models. **Conclusion:** These studies suggest that minimal differences in tumor uptake exist at early time points, dependent on the tumor type. However, these differences equalize over time, reaching around 5.0 percentage injected dose per gram at 20 h after injection. These data provide strong support for the introduction of mandatory experimental controls of future macromolecular or nanoparticle-based drugs, particularly regarding the development of targeted radiotracers.

The enhanced permeability and retention (EPR) effect is the mechanism by which high-molecular-weight nontargeted drugs and prodrugs accumulate in tissues with increased vascular permeability, such as in sites of inflammation or cancer. Attributes of the EPR effect were first described in 1986 by Matsumura and Maeda (1). In their landmark study, the increased tumor uptake and retention of the proteinaceous anticancer drug styrene-maleic acid polymer-functionalized neocarzinostatin (molecular weight [MW], ~16 kDa) was explained by the binding of styrene-maleic acid polymer-functionalized neocarzinostatin to plasma albumin (MW, ~67 kDa). Compared with the native small-molecule neocarzinostatin, this albumin-bound macromolecular drug (MW, ~83 kDa) displayed increased delivery to, and concentration in, the tumor, with prolonged duration of action and increased therapeutic efficacy. The generality of the EPR effect and its dependence on molecular size was demonstrated further by the encapsulation of styrene-maleic acid polymer-functionalized neocarzinostatin in Lipiodol (ethiodized poppyseed oil) liposomes (2)—a result that fueled research interest in liposomal formulations as drug delivery vehicles for anticancer chemotherapeutics (3–8).

From a physiologic perspective, the EPR effect is specific in that it occurs only in tissues that display abnormal vasculature such as the microenvironment of tumors. Yet in terms of biochemistry, the EPR effect depends only on global properties including molecular size, shape, charge, and polarity and is independent of any targeted or specific binding properties such as ligand–receptor interactions.

It is important to note that the EPR effect is different from the nontargeted, passive uptake of small molecules by diffusion in diseased tissues (9). The principal difference

---

between EPR and passive localization lies in the characteristics of retention and tissue clearance rather than uptake. Small molecules rapidly penetrate the interstitial space of tumors, but in the absence of specific binding to cellular proteins, cellular uptake, or metabolism, the drug is not retained and may be free to diffuse out of the tissue back into the blood pool or lymphatic system. In contrast, macromolecules have smaller diffusion constants that, on the one hand, reduce the initial rate of tumor uptake but, on the other, also tend to increase the half-life of blood-pool circulation, enhance tissue retention, and greatly decrease the rate of clearance. By way of example, the vascular permeability dye Evans blue (which forms a noncovalent, macromolecular complex with albumin) was shown to have a decreased rate of clearance from tumor tissue (>3–4 wk), compared with healthy tissue (<1 wk) (1).

Despite advances over the last 25 years in our understanding of the nature of the EPR effect, important questions remain. What is the influence of tumor size and phenotype on the EPR effect? To what extent does tissue perfusion, vascularity, and necrosis influence drug uptake by the EPR effect? For a given molecule, how does the EPR effect contribute to accumulation of the drug in the target tissue over time? Furthermore, with the growth of nanotechnology for potential use in biomedical applications, there is an immediate requirement to ensure rigorous evaluation of the efficacy of these new constructs. Any given class of macromolecule with characteristic size, shape, charge, polarity, and lipophilicity will show tumor uptake to a certain extent via the EPR effect. In molecular targeting, this lower limit has to be exceeded to visualize specific binding of the radiotracer. Numerous multimodality nanoparticle-based agents such as functionalized carbon nanotubes, liposomes, macromolecular proteins, nucleic acid polymers, dendrimers, aptamers, iron-oxide particles, and quantum dots have been reported to accumulate in tumors. However, the question of whether this uptake is specific for the intended target is not always addressed.

Answering all of the aforementioned questions is clearly beyond the scope of a single research article. Rather, in this work we examined whether the magnitude of the EPR effect with reference to radiotracer uptake in tumors correlates with different tumor sizes and phenotypes. We investigated the in vivo distribution of ^{89}Zr-labeled mouse serum albumin (^{89}Zr-mAlb) because albumin is, in general, known to accumulate in inflamed tissues and tumors via the EPR effect (10,11). Therefore, mAlb can serve as a macromolecular radiopharmaceutical displaying quantifiable uptake in 3 well-established xenograft models of human prostate cancer. Tumor models focus on 3 commonly used human prostate cancer lines of different origins, CWR22rv1, DU-145, and PC-3. Experiments include the use of PET, ex vivo biodistribution, contrast-enhanced ultrasound (CEUS) imaging, histology, and autoradiography to probe the influence of tumor size and phenotype on the magnitude of the EPR effect.

MATERIALS AND METHODS

Full details of all methods and equipment used are presented in the supplemental materials (available online only at http://jnm.snmjournals.org).

Protein Modification and Radiolabeling

mAlb (Sigma-Aldrich) was functionalized with the chelate desferrioxamine B (DFO; Calbiochem) using previously described procedures (supplemental materials).

^{89}Zr was produced via the ^{89}Y$(p,n)^{89}$Zr transmutation reaction on a TR19/9 variable-beam energy cyclotron (Ebco Industries Inc.) in accordance with previously reported methods (12,13).

^{89}Zr-DFO-mAlb was prepared by the complexation of ^{89}Zr-oxalate with DFO-mAlb. Typical radiolabeling reactions were conducted in accordance with previously reported methods used for labeling monoclonal antibodies (mAbs) with ^{89}Zr (supplemental materials) (14,15).

Stability Studies

The stability of ^{89}Zr-DFO-mAlb with respect to change in radiochemical purity or loss of radioactivity from the protein was investigated in vitro by incubation in solutions of saline and phosphate-buffered saline for 7 d at room temperature and 37°C. Radiochemical purity was determined by radio–instant thin-layer liquid chromatography, γ-counting, and analytic size-exclusion chromatography (supplemental materials).

Xenograft Models

All animal experiments were conducted in compliance with Institutional Animal Care and Use Committee guidelines. Male athymic *nu/nu* mice (NCRNU-M; weight, 20–22 g; age, 6–8 wk) were obtained from Taconic Farms Inc. and were allowed to acclimatize at the Memorial Sloan-Kettering Cancer Center vivarium for 1 wk before studies were commenced. In each mouse, respective prostate cancer cells were injected subcutaneously, both on the left and on the right flanks for tumor induction (Supplemental Figs. 1 and 2).

Biodistribution Studies

CWR22rv1, DU-145, and PC-3 tumor–bearing mice were randomized before the study and were warmed gently with a heat lamp 5 min before ^{89}Zr-DFO-mAlb (0.55–0.74 MBq [15–20 μCi], 3–4 μg of protein, in 200 μL of sterile saline for injection) was administered via tail vein injection (t = 0 h). Animals (n = 3–5 per group) were euthanized by CO_2 gas asphyxiation at 1, 4, and 20 h after injection, and 16 organs (including the 2 tumors) were harvested, rinsed in water, dried in air for 5 min, weighed, and counted on a γ-counter for accumulation of ^{89}Zr radioactivity (supplemental materials).

Small-Animal PET

PET experiments were conducted on a microPET Focus 120 scanner (Concorde Microsystems). Mice were administered ^{89}Zr-DFO-mAlb formulations (3.40–3.52 MBq [92–95 μCi], 19.5–21.5 μg of protein, in 200 μL of sterile saline for injection) via tail vein injection. Approximately 5 min before PET images were recorded, mice were anesthetized by inhalation of 1%–2% isoflurane (Baxter Healthcare)–oxygen gas mixture and placed on the scanner bed. PET images were recorded at 1, 4, and 20 h after injection. Before euthanasia by CO_2 gas asphyxiation, 100 μL of a 1% Evans blue solution was administered via tail vein injection. Tumors were resected and preserved fresh frozen for histologic analysis (supplemental materials).

Ultrasound

Ultrasound imaging was conducted on a Vevo 770 device (VisualSonics Inc.) equipped with RMV-710B and RMV-708 scan heads. Automated 3-dimensional stacks of the tumors were acquired in B mode for morphologic analysis and tumor volumetry. CEUS was performed after bolus injections of 100 μL of commercially available microbubbles (Micromarker Kit 1; VisualSonics) via tail vein catheters according to established protocols (16). Destruction–replenishment curves were recorded and analyzed. Additionally, automated 3-dimensional stacks were obtained in power Doppler mode after microbubble injection (supplemental materials).

Digital Autoradiography (DAR) and Histology

Serial 10-μm-thick sections were cut at −20°C in an HM 500 M cryostat (Microm) at different levels of each tumor and immediately deposited onto a glass plate. DAR was performed with a FujiFilm BAS-1800 II device (Fuji Photo Film) for 24 and 36 h. Region-of-interest–based density analysis was performed with the Multi Gauge software (Fujifilm Medical Systems). Intravital Evans blue staining was visualized on nonfixed slices with a BX 60 microscope (Olympus America) equipped with a 10×/0.30 UPlanF objective, a ProScan II automated stage (Prior Scientific Instruments), and a CC12 Soft Imaging Systems camera (Olympus America). Microsuite Five software (Olympus America) was used to align the individual image frames and render these into a single montage of the entire tumor section. Subsequently, hematoxylin and eosin staining (H&E) was performed to visualize tumor morphology. Images of H&E-stained sections were acquired in a similar manner.

Statistical Analysis

Data were plotted and analyzed with the nonparametric Wilcoxon test using the JMP software (SAS Institute Inc.). Differences at the 95% confidence level ($P < 0.05$) were considered to be statistically significant.

RESULTS

Choice of Radiotracer

Before rational experiments investigating quantitative and phenotypic characteristics of the EPR effect could be conducted from a radiochemistry perspective, we first needed to develop a suitable radiotracer. Because the EPR effect is defined by the nonspecific uptake and retention of a macromolecule, it was essential that the radiotracer be large (MW, >40 kDa) and have no affinity for potential tumor receptors. Therefore, in these preliminary studies, mAlb (MW, ~67 kDa) was selected because it is a large globular protein of sufficient size, the protein is native and ubiquitous to the mouse models used and has a high concentration in blood plasma (~36 mg/mL) (17), it can be radiolabeled without deleterious changes to its topological structure, it does not have a known target receptor protein in human xenografts of prostate cancer, and its high endogenous levels in serum means that in our experimental design we are always working under the condition of extremely low specific activity, thereby negating any possible effects of specific receptor binding and ensuring the uptake observed is due to nonspecific EPR effects.

Although the precise biochemical pathways of Zr(IV) ions in mammals remain uncertain, [89]Zr was selected as the radionuclide because our previous studies have demonstrated excellent PET image contrast with high in vivo stability, limited (if any) metabolism, high retention in target tissue, and low background accumulation in normal tissues (12,14,15,18). High in vivo stability is an essential property for these experiments on EPR quantification because radiotracer metabolism and potential recirculation of the radionuclide (as is common with, for example, iodine-based radiotracers) would complicate analysis.

Radiochemistry

mAlb was functionalized with the DFO chelate using methods developed from studies on [89]Zr labeling of mAbs (12,14,15). As expected, radiolabeling of DFO-mAlb with [89]Zr-oxalate was found to be facile at room temperature in aqueous solutions at pH 7.7–8.3. Crude [89]Zr-DFO-mAlb was purified from small-molecule impurities using spin-column centrifugation. In a typical reaction, the final radiochemical yield of purified [89]Zr-DFO-mAlb was more than 80%, and the product was formulated in sterile saline with a radiochemical purity of more than 99% ($n = 4$) and a specific activity of 160.2 ± 4.6 MBq/mg (4.33 ± 0.12 mCi/mg). Isotopic dilution assays revealed an average of 2.1 ± 0.3 accessible chelates per protein molecule (14,15,19). In vitro stability studies were consistent with previous reports on the stability of [89]Zr-mAbs (18). [89]Zr-DFO-mAlb was found to be stable with respect to loss of the radionuclide from the protein for up to 7 d at room temperature and 37°C in both saline and phosphate-buffered saline and was deemed suitable for further evaluation in vivo.

PET with [89]Zr-DFO-mAlb

Initial PET experiments were conducted to verify that [89]Zr-DFO-mAlb localized and accumulated in CWR22rv1, DU-145, and PC-3 human prostate xenografts (Fig. 1). [**Fig. 1**] These tumor lines were selected because they were derived from prostate tumor tissue of different origins (CWR22rv1, primary tumor; DU-145, brain metastasis; and PC-3, bone metastasis) and represent well-established models of prostate cancer with known growth rates and reproducible inoculation take rates. They display a suitable range of genotypic and phenotypic differences including androgen dependency and surface-marker expression (20–23). The temporal PET images demonstrate that CWR22rv1 tumors can be visualized above background within 1 h after intravenous administration of [89]Zr-DFO-mAlb. Radiotracer uptake and retention in the tumors show a characteristic increase from 1 to 4 h and a continued increase for up to more than 20 h. The PET images indicate a heterogeneous intratumoral uptake of [89]Zr-DFO-mAlb in all 3 xenograft models. Furthermore, this heterogeneous uptake changes over time (CWR22rv1 PET images at 1, 4, and 20 h) and appears to be different for each of the tumor phenotypes studied. Overall, the PET experiments confirm that the EPR effect is operational for [89]Zr-DFO-mAlb localization and accumulation in CWR22rv1, DU-145, and PC-3 tumors.

Biodistribution Studies

After confirming that ^{89}Zr-DFO-mAlb accumulates in CWR22rv1, DU-145, and PC-3 xenografts, we conducted full ex vivo biodistribution studies at 1, 4, and 20 h after intravenous administration ($n = 3$ or 4 per group for each time point) to gain accurate quantitative data on radiotracer uptake in tumors (number of tumors = $2n$/group). Importantly, each group of animals contained a range of tumor sizes so that the dependence of radiotracer uptake on tumor size could be evaluated. Selected biodistribution data are presented in Table 1, and radiotracer accumulation in the blood pool and tumors and time–activity curves of tumor-to-blood ratios are plotted in Figure 2.

The change in blood-pool ^{89}Zr-activity was consistent across each of the 3 tumor models throughout the course of the experiment (Table 1). The data demonstrate higher uptake in CWR22rv1 tumors than in DU-145 and PC-3 xenografts after 1 h (2.7 ± 0.5, 2.0 ± 0.3, and 1.5 ± 0.5 percentage injected dose per gram [%ID/g], respectively). Although absolute uptake was low, the differences observed among tumor phenotypes were found to be statistically significant ($P < 0.001$, for all comparisons). At later time points, despite extraction from the blood pool and some renal excretion or kidney uptake, ^{89}Zr-DFO-mAlb uptake in CWR22rv1, DU-145, and PC-3 xenografts continued to increase, reaching 4.4 ± 0.8, 3.6 ± 0.6, and 3.7 ± 0.8 %ID/g at 4 h, and 5.2 ± 1.2, 4.2 ± 0.7, and 5.2 ± 0.8 %ID/g at 20 h after administration, respectively, with no significant differences among the 3 tumor models. This increased tumor uptake and retention of ^{89}Zr-DFO-mAlb at late time points is consistent with the EPR mechanism, whereby extravasation of the radiotracer from the blood pool into the interstitial tissue occurs.

Sonographic Morphology

Ultrasound imaging showed oval lesions with well-defined borders and heterogeneous echo patterns (Figs. 3; Supplemental Figs. 1 and 2). Hypoechoic areas compatible with necrosis were most pronounced in CWR22rv1 tumors and least apparent in PC-3 tumors. Some tumors showed central, echoless areas consistent with necrotic cores.

To account for differences in tumor biology in differently sized lesions, the aim of this study was to investigate a large range of tumor volumes. Tumor sizes in vivo were confirmed by tumor volumetry (CWR22rv1, 63–903 mm^3; DU-145, 33–438 mm^3; and PC-3, 32–163 mm^3). Statistical analysis of the ultrasound data revealed significant differences among all 3 tumor types, with mean tumor volumes of CWR22rv1 > DU-145 > PC-3.

Tumor Perfusion

Two different techniques have been used to characterize the vascular bed of the different xenografts: power Doppler imaging and destruction–replenishment curve analysis using CEUS.

Power Doppler imaging visualizes the blood flow in vessels with diameters larger than 100 μm. Three-dimensional power Doppler analysis of the ultrasound data revealed no differences among the 3 xenograft types.

Destruction–replenishment curves are used for visualization of the microvascular bed. In brief, microbubbles are injected, staying strictly intravascular and increasing the ultrasound signal by enhanced backscattering. Once a plateau is reached, the microbubbles are destroyed within the field of view by a strong ultrasound pulse. The replenishment of the microbubbles is recorded, and the data are fitted with an exponential curve, $VI = \alpha(1 - e^{-\beta t})$, where α is an estimation of the microvascular cross-sectional area, and β reflects microbubble velocity (16).

The microvascular cross-sectional area was found to be the highest for DU-145 tumors and lowest for PC-3 xenografts, with statistically significant differences among all 3 tumor types (Table 2). No differences were found for microbubble velocity among the different cell lines.

Analysis of maximum-intensity-projection images of the contrast cine loops revealed that contrast enhancement could be detected in about 70% of the area of DU-145 and PC-3 xenografts and in about 50% of the area of CWR22rv1 tumors. The areas without contrast enhancement were consistent with the hypoechogenic regions found in B mode imaging and consequently correspond to nonperfused necrotic zones.

FIGURE 1. Representative coronal and transverse PET images showing ^{89}Zr-DFO-mAlb radiotracer uptake in mice bearing contralateral CWR22rv1, DU-145, or PC-3 human prostate xenografts on lower left and right flanks. For mouse bearing CWR22rv1 tumors, temporal PET images recorded at 1, 4, and 20 h after intravenous administration of radiotracer are presented to demonstrate change in radiotracer biodistribution and image contrast over time. White lines indicate approximate level of coronal or transverse slice. H = heart; Ki = kidney; L = Liver; T = tumor; Trans. = transverse.
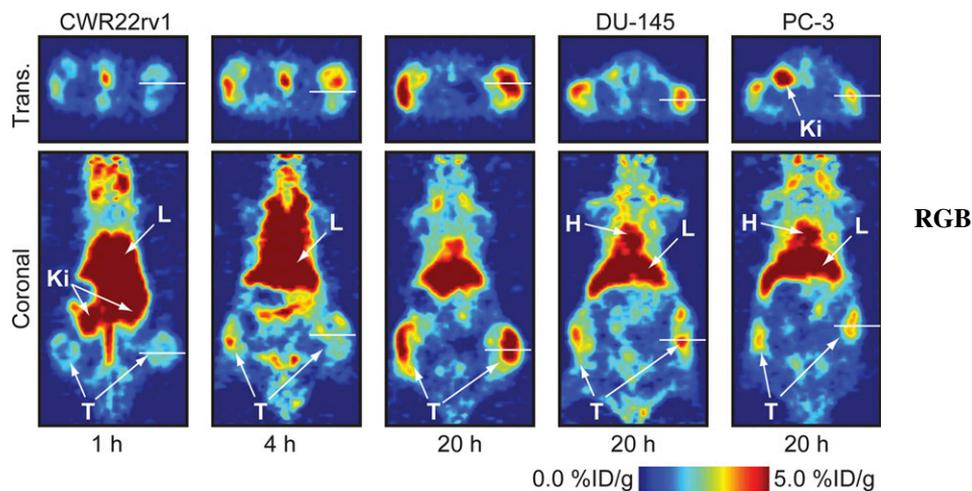
TABLE 1
Biodistribution Data Showing Uptake of ^{89}Zr-DFO-mAlb in Selected Tissues Versus Time (Hour), in Tumor-Bearing Mice

Organ	CWR22rv1			DU-145			PC-3		
	1 h (n = 3)	4 h (n = 3)	20 h (n = 3)	1 h (n = 3)	4 h (n = 3)	20 h (n = 4)	1 h (n = 3)	4 h (n = 3)	20 h (n = 4)
Blood	30.0 ± 2.1	21.3 ± 1.0	8.8 ± 0.4	28.0 ± 1.3	21.0 ± 1.2	7.9 ± 0.7	27.6 ± 2.0	17.3 ± 2.0	8.6 ± 0.8
Tumor*	2.7 ± 0.5	4.4 ± 0.8	5.2 ± 1.2	2.0 ± 0.3	3.6 ± 0.6	4.2 ± 0.7	1.5 ± 0.5	3.7 ± 0.8	5.2 ± 0.8
Heart	9.9 ± 1.1	6.4 ± 0.4	4.1 ± 0.3	8.3 ± 0.8	7.0 ± 0.4	4.3 ± 0.9	10.5 ± 3.2	5.4 ± 0.1	4.3 ± 0.5
Lungs	17.7 ± 4.0	17.7 ± 2.8	5.4 ± 0.7	20.3 ± 1.4	17.5 ± 4.9	6.2 ± 1.3	19.9 ± 0.8	15.8 ± 1.0	5.3 ± 0.5
Liver	13.3 ± 1.3	11.3 ± 0.5	11.7 ± 0.3	10.7 ± 0.6	12.4 ± 0.8	11.2 ± 0.8	10.1 ± 1.9	9.6 ± 0.7	9.2 ± 1.1
Spleen	5.4 ± 0.7	6.0 ± 0.4	6.1 ± 1.2	4.4 ± 0.5	6.1 ± 0.6	5.8 ± 0.3	4.7 ± 1.0	5.4 ± 0.4	5.5 ± 0.2
Pancreas	2.0 ± 0.4	1.9 ± 0.3	1.2 ± 0.3	1.6 ± 0.1	1.9 ± 0.1	1.2 ± 0.2	1.8 ± 0.1	1.5 ± 0.2	1.2 ± 0.03
Stomach	1.2 ± 0.3	1.4 ± 0.02	0.8 ± 0.2	0.9 ± 0.04	1.3 ± 0.2	0.7 ± 0.1	0.8 ± 0.1	1.0 ± 0.2	0.5 ± 0.2
Small intestine	3.3 ± 0.2	2.8 ± 0.2	2.1 ± 0.5	2.6 ± 0.2	2.9 ± 0.3	1.8 ± 0.2	2.9 ± 0.3	2.1 ± 0.2	1.6 ± 0.2
Large intestine	0.7 ± 0.1	1.0 ± 0.2	1.3 ± 0.1	0.5 ± 0.1	1.3 ± 0.6	1.2 ± 0.2	0.9 ± 0.3	1.3 ± 0.1	1.0 ± 0.2
Kidneys	13.0 ± 2.1	13.0 ± 0.7	17.9 ± 2.5	11.2 ± 0.7	14.1 ± 0.9	15.3 ± 1.2	12.1 ± 1.6	10.9 ± 1.0	15.4 ± 0.3
Muscle	0.8 ± 0.1	1.1 ± 0.3	1.4 ± 0.4	0.6 ± 0.1	0.9 ± 0.2	0.9 ± 0.2	0.6 ± 0.2	0.8 ± 0.2	0.7 ± 0.1
Bone	2.3 ± 0.3	2.5 ± 0.5	2.9 ± 0.8	2.1 ± 0.4	3.0 ± 0.7	2.5 ± 0.2	2.3 ± 0.4	2.5 ± 0.6	2.2 ± 0.2
Fat	1.8 ± 0.1	1.6 ± 1.0	2.1 ± 0.9	0.5 ± 0.1	2.0 ± 0.6	1.6 ± 0.7	0.7 ± 0.3	0.9 ± 0.3	1.2 ± 0.4
Testes	2.6 ± 0.3	2.7 ± 0.05	2.5 ± 0.4	2.0 ± 0.2	2.4 ± 0.8	2.5 ± 0.3	2.9 ± 0.1	2.5 ± 0.2	2.5 ± 0.2
T/B ratio†	0.09 ± 0.02	0.21 ± 0.04	0.59 ± 0.13	0.07 ± 0.01	0.17 ± 0.03	0.53 ± 0.10	0.05 ± 0.02	0.21 ± 0.05	0.60 ± 0.11

*Tumor uptake values are average and SD of 2n tumors, where n is number of animals per group.
†Tumor-to-blood ratio; errors are calculated as geometric mean of SD.
Complete biodistribution data are presented in supplemental materials. Data are expressed as mean %ID/g ± SD.
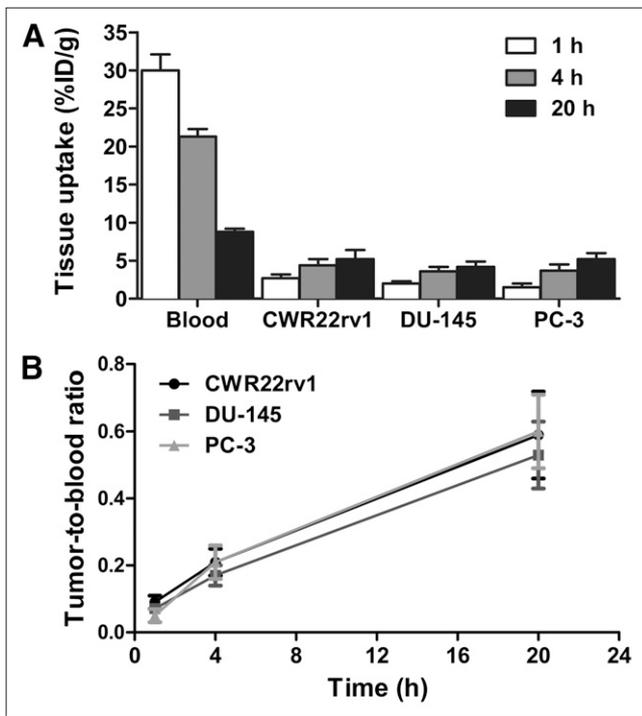
FIGURE 2. (A) Bar chart showing change in ^{89}Zr-DFO-mAlb uptake in blood pool (representative data for CWR22rv1 models shown) and 3 tumor models over time (h). (B) Tumor-to-blood time–activity contrast curves.

Histology and Autoradiography

Histologic staining, DAR, and microscopy were performed to gauge the potential dependence of ^{89}Zr-DFO-mAlb uptake on tumor perfusion, vascularization, and necrosis and the influence of phenotypic differences among the CWR22rv1, DU-145, and PC-3 xenograft models on radiotracer uptake [Fig. 4] by the EPR effect. Figure 4 shows representative microscopy images for H&E staining (purple), DAR (green), and albumin-bound Evans blue fluorescence emission (red) from adjacent slices of CWR22rv1, DU-145, and PC-3 tumors. Tumors were harvested 20 h after radiotracer administration and 10–15 min after intravenous Evans blue administration. Evans blue dye is known to form a noncovalent macromolecular complex with serum albumin, which is stable in vivo for an extended time (>4 wk) (1).

H&E staining demonstrated marked differences among all 3 tumor models. CWR22rv1 xenografts showed large regions of necrosis partially with cystic areas surrounded by streaks of tumor cells, whereas PC-3 tumors showed a more homogeneous pattern, with thinned-out tumor tissue in some regions indicating the start of necrosis development. DU-145 xenografts displayed necrotic areas with cystic transformation but also large parts of regularly developed tumor tissue. Therefore, H&E staining suggests that the degree of necrosis increases in the order CWR22rv1 > DU-145 > PC-3. These results are consistent with the ultrasound morphology.

DAR at 20 h after radiotracer administration showed distinct localization of the ^{89}Zr radioactivity in necrotic
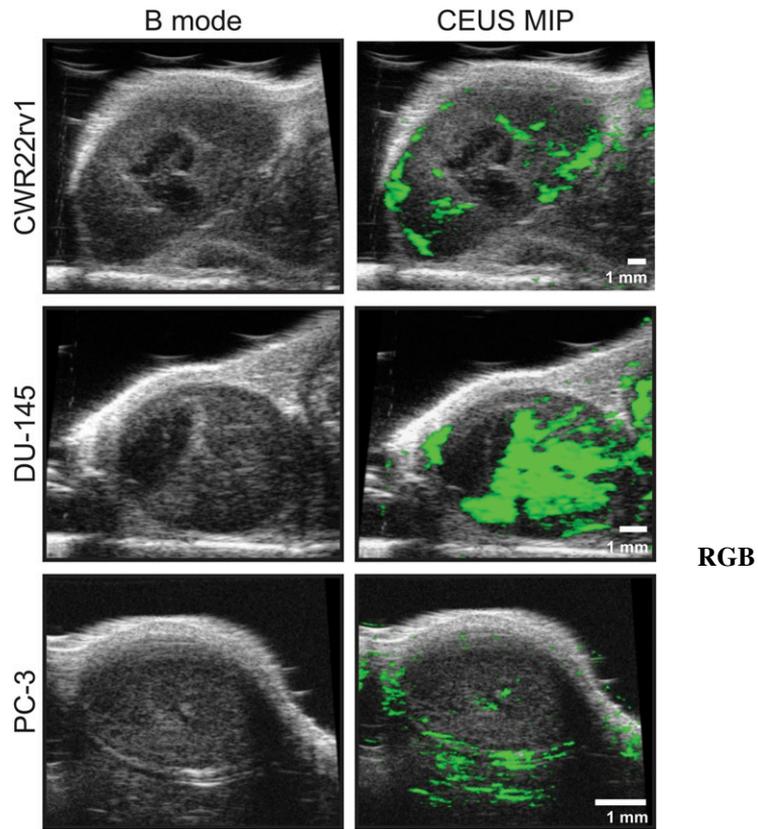

RGB

FIGURE 3. B mode (left) and CEUS maximum-intensity-projection images (right) of representative CWR22rv1, DU-145, and PC-3 tumors. B mode images show heterogeneous echo patterns with hypoechogenic and echo-free areas consistent with necrotic zones. CEUS maximum-intensity-projection data depict differences in vascularization among the 3 tumor types; signal increase due to microbubble presence is coded as green. MIP = maximum intensity projection.

regions of each tumor type, with little activity in the histologically undisturbed parts of the tumor. Region-of-interest–based density analysis showed no difference among the tumor models (data not shown)—a finding consistent with the results of the biodistribution. DAR data at 20 h are broadly assigned to nonspecific extravasation of ^{89}Zr-DFO-mAlb and tumor uptake by EPR.

In contrast to the ^{89}Zr-DFO-mAlb DAR data, the distribution of the Evans blue staining in the same tumors is correlated to perfusion and vascularization of the tissue and not uptake by the EPR effect because the dye was allowed to circulate for only 10–15 min before sacrifice. These images (Fig. 4) showed extensive fluorescence in DU-145 xenografts, indicating high vascular densities in these tumors. CWR22rv1 xenografts showed high staining intensities in the nonnecrotic parts of the tumors, whereas PC-3 xenografts displayed only weak staining concentrated on the tumor margins. These data indicate vascular cross-sectional areas of DU-145 > CWR22rv1 > PC-3 xenografts, as is consistent with the CEUS data. Early-time-point Evans blue staining shows no uptake in the necrotic regions in any of the 3 tumor phenotypes.

Tumor	α (signal intensity)*		β (1/s)†		Percentage of vascularity (%)	
	Median	Confidence interval	Median	Confidence interval	Median	Confidence interval
CWR22rv1	8.9	2.8	0.3	0.2	0.72	1.05
DU-145	39.0	12.6	0.2	0.1	1.87	1.59
PC-3	6.1	1.1	0.4	0.1	0.85	0.66

*α reflects microvascular cross-sectional area.
†β reflects microbubble velocity.

DISCUSSION

The EPR mechanism of accumulation and retention in tissues with disrupted vasculature is a well-established phenomenon and is an important strategy for delivering macromolecular drugs to sites of disease (*9*). With the increased scope and prevalence in the use of targeted nanoparticle materials and large proteins in medical research, it is imperative to understand the quantitative contribution of the EPR effect in drug accumulation to ensure both accurate assessment of a potential drug's selectivity, specificity, and efficacy and the correct measurement and prediction of dosing limits.

Of particular importance to the field of radiochemistry is the answer to the following question: for a given class of molecules, what is the minimum level of uptake required before a targeted radiotracer can be declared to be specific? For common studies on, for example, radiolabeled mAbs or targeted proteins, the in vivo reactivity and specificity for the target epitope or receptor is usually demonstrated by the following: competitive inhibition (blocking) experiments using low-specific-activity formulations or an exogenous inhibitor, comparison of the specific uptake of a radiotracer (e.g., an IgG_1) with that observed using a nonspecific isotype control (e.g., an equivalent, nonspecific IgG_2), direct comparison of the difference in target-tissue uptake observed between a specific radiotracer and an equivalent radiotracer with a scrambled binding sequence (e.g., targeted peptides vs. a scrambled peptide sequence), or the use of knockout–knockdown models in which target protein expression is modulated at the cellular level. However, these experiments are not always performed in reported work, leading to difficulty in drawing conclusions about the specificity and selectivity of any new radiotracer or drug molecule.

Our studies demonstrate that CWR22rv1, DU-145, and PC-3 prostate tumor models can be visualized by radiotracer accumulation by the EPR effect alone. Quantitative PET and ex vivo biodistribution studies are self-consistent and suggest that, despite the high degree of intra- and intertumoral heterogeneity found in tumor vascularity and necrosis for the xenograft models investigated, nonreceptor specific localization and retention of [89]Zr-DFO-mAlb

reaches 5.0 %ID/g at 20 h after administration in all models. However, at early time points, that is, 1 h after injection, statistically significant differences were found among the 3 tumor types, showing [89]Zr-DFO-mAlb tumor uptake in the order CWR22rv1 > DU-145 > PC-3. These differences correlate with the areas of necrosis as determined sonomorphologically and via H&E staining. Because the differences described in [89]Zr-DFO-mAlb uptake are equalized as early as 4 h after injection, it is tempting to speculate that the diffusion of the radiotracer out of the vasculature into the tumors occurs more quickly in highly necrotic tumors than in less necrotic tumors.

It has been described that tumor cells take up albumin as a source for energy and amino acids, and albumin conjugated to cytotoxic drugs has even proven useful for chemotherapeutic purposes (*24,25*). However, in our study the concentration of [89]Zr-DFO-mAlb activity was highest in necrotic regions and less in viable tumor areas at later time points (>20 h; Fig. 4), indicating that uptake of [89]Zr-DFO-
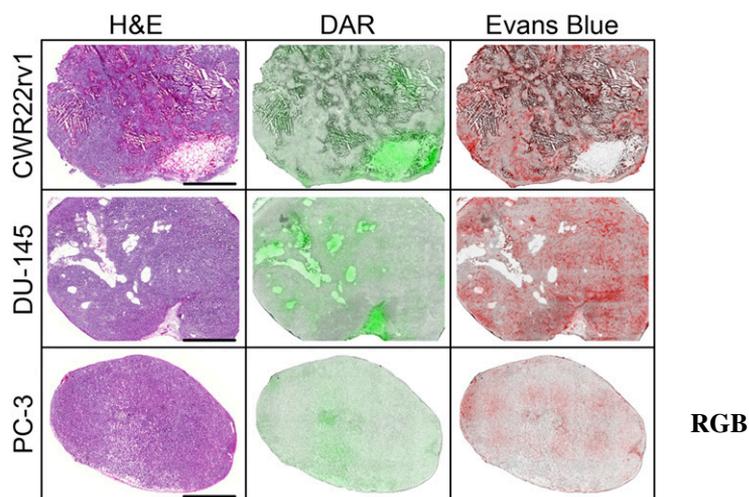

RGB

FIGURE 4. Microscopy images of adjacent histologic CWR22rv1, DU-145, and PC-3 tumor tissue slices stained with H&E (purple), albumin-bound Evans blue (fluorescence image; red), and DAR (green) showing intratumoral distribution of [89]Zr-DFO-mAlb. Tumors were harvested and fresh frozen at 20 h after intravenous administration of radiotracer. Evans blue dye was administered intravenously 10–15 min before sacrifice. Scale bar = 2 mm.

mAlb into the tumor cells may indeed contribute to the overall amount of uptake, but it is not the major mechanism for radiotracer accumulation in our model systems. Rather, we speculate that accumulation in the necrotic areas may be due to clearance by the lymphatic system in the perfused tumor regions, but further studies are required to provide experimental evidence for this mechanism. Interestingly, despite dependence of radiotracer uptake on tumor phenotype at early time points, by the time the EPR effect begins to dominate the distribution, and a balance between blood-pool and tumor tissue activity is reached, phenotypic differences are found to play a less important role in the overall radiotracer retention.

Tumor size was found to have limited influence on radiotracer uptake at all time points. This is to be expected because it is known that tumors as small as 100 μm in diameter can have well-developed microvessel networks, regions of necrosis, and high expression of proangiogenic factors (26–28). Hence, for most practical studies, these experiments indicate that tumor size is not expected to influence the magnitude of the EPR effect on measured radiotracer uptake. However, it is noted that excessively large tumors with dead or necrotic cores will affect the specific uptake of targeted radiotracers, and this heterogeneity is especially important if tumor tissue is divided for separate studies (e.g., half for biodistribution and half for histology).

On the basis of the mechanism of EPR and our preliminary studies reported here, we propose that the specificity of any targeted macromolecular radiotracer or drug molecule must be demonstrated by experiment before the compound is evaluated for therapeutic or diagnostic efficacy. We submit that the target-tissue accumulation by EPR effect should be determined as a minimum threshold value, with a scrambled or nontargeted analog of the targeted radiotracer in addition to competition studies to describe the uptake of a targeted macromolecular or nanoparticle-based radiotracer as high or specific. This threshold will almost certainly depend on molecular size, shape, charge and polarity, lipophilicity, and radiotracer stability with respect to metabolism or loss of the radionuclide and should be identified for each new class of targeted radiotracer. ^{89}Zr-DFO-mAlb, a globular protein around 67 kDa in size, reached a minimum threshold value of around 5.0 %ID/g at approximately 20 h and may provide a point of reference applicable to most medium-sized protein-based agents. Additionally, the methods used in this work can be easily translated to studies involving different mouse models, tumor phenotypes, or molecular entities.

CONCLUSION

The EPR effect plays an important role in tumor uptake of macromolecules at late investigational time points. At early time points (<1 h after administration), radiotracer and other drug uptake is dominated by vascularization and the degree of necrosis of solid tumors and is therefore dependent on tumor phenotype. By 20 h, histologic studies showed that intratumoral distribution of nonspecific radio-tracers or drugs is likely to be focused on regions of necrosis as opposed to vascularized areas. Furthermore, at late time points differences in tumor phenotype are found to have a minimal role in defining peak radiotracer accumulation. Biodistribution studies demonstrated that at 20 h, nonspecific tumor uptake of ^{89}Zr-DFO-mAlb by the EPR effect in CWR22rv1, DU-145, and PC-3 xenograft models reached the same magnitude of around 5.0 %ID/g. We suggest that the minimum level of accumulation via EPR effect be determined for any new targeted macromolecular and nanoparticle-based radiotracer before the observed experimental uptake is described as high, specific, or selective.

REFERENCES

1. Matsumura Y, Maeda H. A new concept for macromolecular therapeutics in cancer chemotherapy: mechanism of tumoritropic accumulation of proteins and the antitumor agent smancs. *Cancer Res.* 1986;46:6387–6392.
2. Maeda H. SMANCS and polymer-conjugated macromolecular drugs: advantages in cancer chemotherapy. *Adv Drug Deliv Rev.* 2001;46:169–185.
3. Maeda H, Seymour LW, Miyamoto Y. Conjugates of anticancer agents and polymers: advantages of macromolecular therapeutics in vivo. *Bioconjug Chem.* 1992;3:351–362.
4. Yokoyama M, Okano T, Sakurai Y, Kataoka K. Improved synthesis of adriamy-cin-conjugated poly (ethylene oxide)-poly (aspartic acid) block copolymer and formation of unimodal micellar structure with controlled amount of physically entrapped adriamycin. *J Control Release.* 1994;32:269–277.
5. Duncan R. Development of HPMA copolymer-anticancer conjugates: clinical experience and lessons learnt. *Adv Drug Deliv Rev.* 2009;61:1131–1148.
6. Zalipsky S, Saad M, Kiwan R, Ber E, Yu N, Minko T. Antitumor activity of new liposomal prodrug of mitomycin C in multidrug resistant solid tumor: insights of the mechanism of action. *J Drug Target.* 2007;15:518–530.
7. Maeda H, Sawa T, Konno T. Mechanism of tumor-targeted delivery of macromolecular drugs, including the EPR effect in solid tumor and clinical overview of the prototype polymeric drug SMANCS. *J Control Release.* 2001;74:47–61.
8. Torchilin V. Tumor delivery of macromolecular drugs based on the EPR effect. *Adv Drug Deliv Rev.* March 18, 2010 [Epub ahead of print].
9. Maeda H. Tumor-selective delivery of macromolecular drugs via the EPR effect: background and future prospects. *Bioconjug Chem.* 2010;21:797–802.
10. Levick JR. Permeability of rheumatoid and normal human synovium to specific plasma proteins. *Arthritis Rheum.* 1981;24:1550–1560.
11. Stehle G, Sinn H, Wunder A, et al. Plasma protein (albumin) catabolism by the tumor itself: implications for tumor metabolism and the genesis of cachexia. *Crit Rev Oncol Hematol.* 1997;26:77–100.
12. Verel I, Visser GWM, Boellaard R, Stigter-van Walsum M, Snow GB, van Dongen GAMS. ^{89}Zr immuno-PET: comprehensive procedures for the production of ^{89}Zr-labeled monoclonal antibodies. *J Nucl Med.* 2003;44:1271–1281.

13. Holland JP, Sheh Y, Lewis JS. Standardized methods for the production of high specific-activity zirconium-89. *Nucl Med Biol.* 2009;36:729–739.

14. Holland JP, Caldas-Lopes E, Divilov V, et al. Measuring the pharmacokinetic effects of a novel Hsp90 inhibitor on HER2/*neu* expression in mice using [89]Zr-DFO-trastuzumab. *PLoS ONE.* 2010;5:e8859.

15. Holland JP, Divilov V, Bander NH, Smith-Jones PM, Larson SM, Lewis JS. [89]Zr-DFO-J591 for immunoPET of prostate-specific membrane antigen expression *in vivo*. *J Nucl Med.* 2010;51:1293–1300.

16. Wei K, Jayaweera AR, Firoozan S, Linka A, Skyba DM, Kaul S. Quantification of myocardial blood flow with ultrasound-induced destruction of microbubbles administered as a constant venous infusion. *Circulation.* 1998;97:473–483.

17. Kim J, Bronson CL, Hayton WL, et al. Albumin turnover: FcRn-mediated recycling saves as much albumin from degradation as the liver produces. *Am J Physiol Gastrointest Liver Physiol.* 2006;290:G352–G360.

18. Holland JP, Lewis Jason S. Zirconium-89 chemistry in the design of novel radiotracers for immuno-PET. In: Mazzi U, Eckelman WC, Volkert WA, eds. *Technetium and Other Radiometals in Chemistry and Medicine*. Padova, Italy: Servizi Grafici Editoriali snc; 2010:187–192.

19. Anderson CJ, Schwarz SW, Connett JM, et al. Preparation, biodistribution and dosimetry of copper-64-labeled anti-colorectal carcinoma monoclonal antibody fragments 1A3-F(ab')2. *J Nucl Med.* 1995;36:850–858.

20. Mimeault M, Batra SK. Recent advances on multiple tumorigenic cascades involved in prostatic cancer progression and targeting therapies. *Carcinogenesis.* 2006;27:1–22.

21. Pienta KJ, Abate-Shen C, Agus DB, et al. The current state of preclinical prostate cancer animal models. *Prostate.* 2008;68:629–639.

22. Cheung CP, Yu S, Wong KB, et al. Expression and functional study of estrogen receptor-related receptors in human prostatic cells and tissues. *J Clin Endocrinol Metab.* 2005;90:1830–1844.

23. Niu Y, Yeh S, Miyamoto H, et al. Tissue prostate-specific antigen facilitates refractory prostate tumor progression via enhancing ARA70-regulated androgen receptor transactivation. *Cancer Res.* 2008;68:7110–7119.

24. Burger AM, Hartung G, Stehle G, Sinn H, Fiebig HH. Pre-clinical evaluation of a methotrexate–albumin conjugate (MTX-HSA) in human tumor xenografts in vivo. *Int J Cancer.* 2001;92:718–724.

25. Neumann E, Frei E, Funk D, et al. Native albumin for targeted drug delivery. *Expert Opin Drug Del.* 2010;7:915–925.

26. Brown JM, Giaccia AJ. The unique physiology of solid tumors: opportunities (and problems) for cancer therapy. *Cancer Res.* 1998;58:1408–1416.

27. Brown JM. The hypoxic cell: a target for selective cancer therapy-eighteenth Bruce F. Cain memorial award lecture. *Cancer Res.* 1999;59:5863–5870.

28. Brown JM, Wilson WR. Exploiting tumour hypoxia in cancer treatment. *Nat Rev Cancer.* 2004;4:437–447.